WSR-88D Tornado Intensity Estimates. Part I: Real-Time Probabilities of Peak Tornado Wind Speeds

BRYAN T. SMITH,[a] RICHARD L. THOMPSON,[a] DOUGLAS A. SPEHEGER,[b] ANDREW R. DEAN,[a] CHRISTOPHER D. KARSTENS,[a] AND ALEXANDRA K. ANDERSON-FREY[c]

[a] *NOAA/NWS/NCEP, Storm Prediction Center, Norman, Oklahoma*
[b] *NOAA/NWS, Weather Forecast Office, Norman, Oklahoma*
[c] *Cooperative Institute for Mesoscale Meteorological Studies, University of Oklahoma, Norman, Oklahoma*

(Manuscript received 22 January 2020, in final form 20 September 2020)

ABSTRACT: The Storm Prediction Center (SPC) has developed a database of damage-surveyed tornadoes in the contiguous United States (2009–17) that relates environmental and radar-derived storm attributes to damage ratings that change during a tornado life cycle. Damage indicators (DIs), and the associated wind speed estimates from tornado damage surveys compiled in the Damage Assessment Toolkit (DAT) dataset, were linked to the nearest manual calculations of 0.5° tilt angle maximum rotational velocity V_{rot} from single-site WSR-88D data. For each radar scan, the maximum wind speed from the highest-rated DI, V_{rot}, and the significant tornado parameter (STP) from the SPC hourly objective mesoscale analysis archive were recorded and analyzed. Results from examining V_{rot} and STP data indicate an increasing conditional probability for higher-rated DIs (i.e., EF-scale wind speed estimate) as both STP and V_{rot} increase. This work suggests that tornadic wind speed exceedance probabilities can be estimated in real time, on a scan-by-scan basis, via V_{rot} and STP for ongoing tornadoes.

KEYWORDS: Squall lines; Storm environments; Supercells; Thunderstorms; Tornadoes; Operational forecasting

1. Introduction

From the advent of Doppler radar, there have been various attempts to identify velocity signatures associated with tornadoes (e.g., Zrnić and Doviak 1975; Brown and Lemon 1976; Brown et al. 1978). These efforts accelerated with the installation of the NEXRAD (WSR-88D) network in the United States during the early to mid-1990s (e.g., Burgess et al. 1993; Wood and Brown 1997; Mitchell et al. 1998; Trapp et al. 1999), even though tornadoes are not resolved explicitly in WSR-88D data due to insufficient spatial resolution resulting from beamwidth and range limitations. As of the late 2000s, ''super-resolution'' data (Brown et al. 2005; Torres and Curtis 2007) provided the greater possibility to resolve circulations associated with tornadoes.

Mesocyclone signatures are resolvable in WSR-88D data, but do not necessarily vary in tandem with tornado intensity. Mobile Doppler radar observations (French et al. 2013, 2014; Marquis et al. 2016; Bluestein et al. 2019) show that rapid fluctuations in tornado intensity can occur on spatiotemporal scales unresolvable in WSR-88D data. They have also revealed a wide range of vortex structures associated with tornadoes, ranging from intense, broad mesocyclones (several kilometers wide) down to embedded subvortices (tens of meters wide), which complicate what constitutes a tornado (e.g., Wurman and Kosiba 2013). Damage surveys and mobile radar observations have also shown embedded subvortices (lasting a few seconds to a minute or more) that are responsible for some of the highest ground-relative winds and damage in well-sampled tornadoes (e.g., French et al. 2013; Wakimoto et al. 2016; Bluestein et al. 2018, 2019). To complicate matters further, instantaneous mobile radar observations also may not be directly comparable to the standard 3-s gusts at 10-m elevation used for the enhanced Fujita scale (EF)-scale ratings (Edwards et al. 2013; Wurman et al. 2014), and wind estimates derived from EF-scale damage ratings are not always consistent with near-ground mobile radar observations (Wurman et al. 2013; Snyder and Bluestein 2014).

Ideally, mobile Doppler radar would be available in real time to forecast and warning operations, which could allow real-time estimates of tornado damage swaths. However, such data are not available in real time, and there have been relatively few tornadoes sampled with sufficient spatial and temporal resolution to resolve the majority of subvortex evolutions within tornadoes (e.g., the El Reno, Oklahoma, tornado from 31 May 2013; Wurman et al. 2014; Wakimoto et al. 2016; Bluestein et al. 2018). In the 31 May 2013 El Reno, Oklahoma, tornado, there were multiple instances where near-ground winds from mobile Doppler radars were substantially stronger than wind estimates derived from observed damage. Also there were few potential damage indicators in the areas of most intense near-ground winds. Detailed observations of the Goshen County, Wyoming, tornado of 5 June 2009 also revealed similar structures failing at substantially different winds speeds (Wurman et al. 2013).

Despite the limitations of WSR-88D data to explicitly resolve tornadoes, tornado intensity estimates using WSR-88D data have become a focus of multiple studies in the past decade, with work ranging from well-surveyed tornadoes (e.g., LaDue et al. 2012; Kingfield and LaDue 2015) to comparisons with high-resolution mobile Doppler radar data (e.g., Toth et al. 2013). Though sample sizes were limited in the aforementioned studies, the primary reason to pursue WSR-88D tornado intensity estimates is widespread, real-time availability of the data.

Corresponding author: Bryan T. Smith, bryan.smith@noaa.gov

DOI: 10.1175/WAF-D-20-0010.1

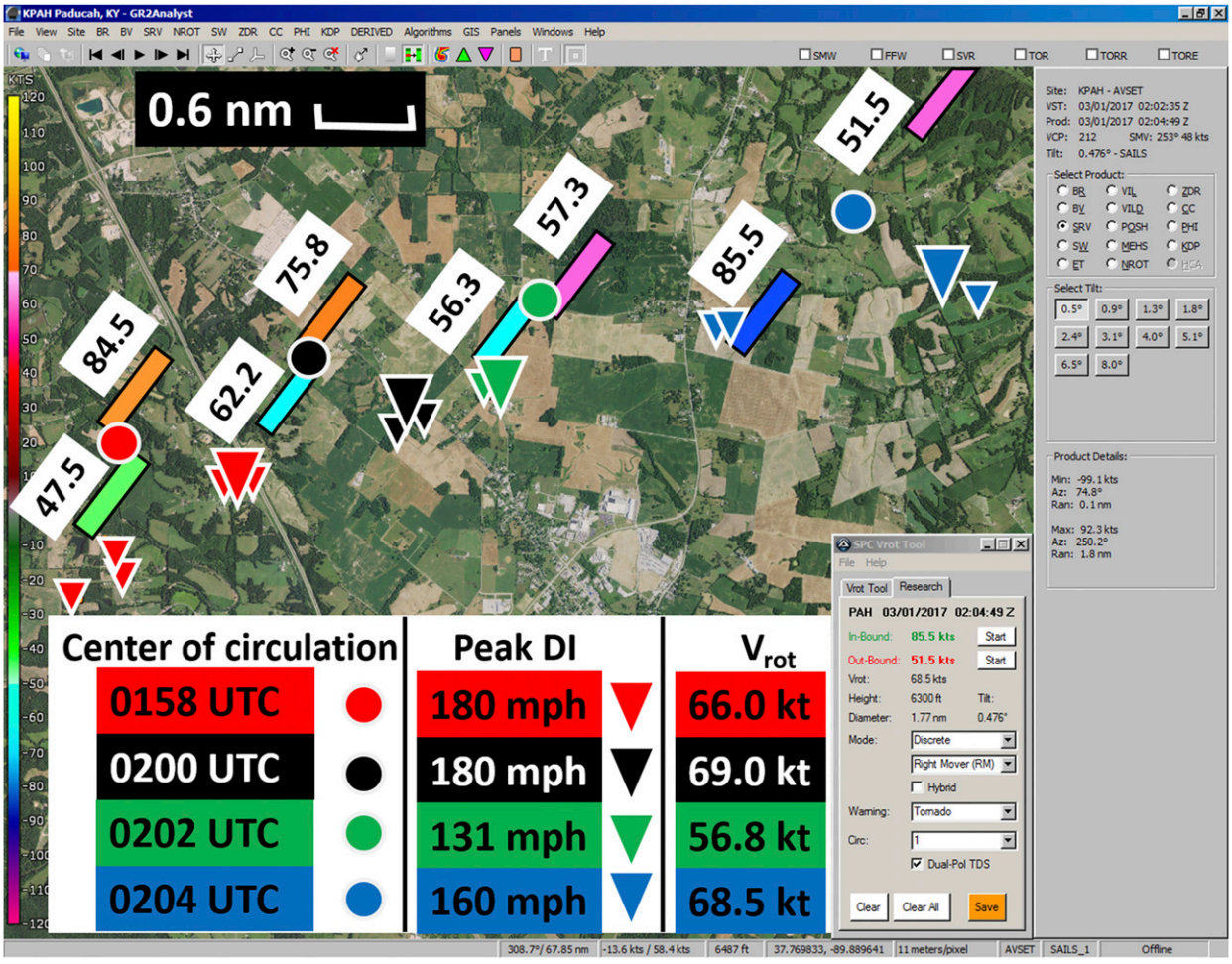

FIG. 1. Landsat imagery with annotated WSR-88D storm-relative velocity (kt; color scale on left) at 0.5° tilt angle from Paducah, KY (KPAH), from 0158 to 0204 UTC 1 Mar 2017. Denoted inserts display the inbound and outbound velocity gates (labeled) used chronologically from left to right to calculate V_{rot} (bottom middle insert). The DIs are geospatially mapped (triangles), assigned to the nearest radar-based circulation center (circle), and color coded to match the velocity scan time (e.g., blue, 0204 UTC; 1 mph = 0.447 m s^{-1}, 1 kt = 0.514 m s^{-1}, 1 n mi = 1.852 km).

More recently, Smith et al. (2015, hereafter S15) constructed a large dataset of tornadoes with associated WSR-88D data for the contiguous United States (2009–13). They demonstrated a clear tendency for manually estimated 0.5° tilt angle maximum rotational velocity V_{rot} to increase with maximum EF-scale damage rating using tornado segment data filtered for the maximum EF-scale rating on a 40-km horizontal grid. Thompson et al. (2017, hereafter T17) extended the work of S15 to include tornadoes (2014–15) and null cases (i.e., non-tornadic severe thunderstorms with identifiable cyclonic V_{rot}) to also estimate tornado probabilities. Thompson et al. (2012), S15, and T17 also included the influence of the near-storm environment on tornado intensity, as represented by the significant tornado parameter (STP)[1] derived from hourly Storm Prediction Center (SPC) analyses at 40-km horizontal grid spacing (Bothwell et al. 2002). In combination, these investigations provided empirical evidence of variations in maximum EF-rating tornado intensity as a function of near-storm environmental conditions on a 40-km hourly grid and peak storm-scale rotation strength during the lifetime of tornadoes.

Real-time estimates of tornado intensity would obviously benefit the severe weather enterprise in general, and augment life-saving information provided by the National Weather Service (NWS). NWS warning procedures rely on WSR-88D scans that are updated every 1.5–5 min, as well as assessments of the near-storm environment and information from weather spotters, emergency management, and the broadcast media. The findings of S15 and T17 appear applicable to NWS warning decisions, though they only considered peak V_{rot} and EF-scale ratings during the entire lifetime of a tornado (i.e., the peak V_{rot} and EF-scale ratings did not necessarily occur during the same radar scans). In support of NWS warning operations, a

[1] STP effective-layer calculation with convective inhibition (Thompson et al. 2012).

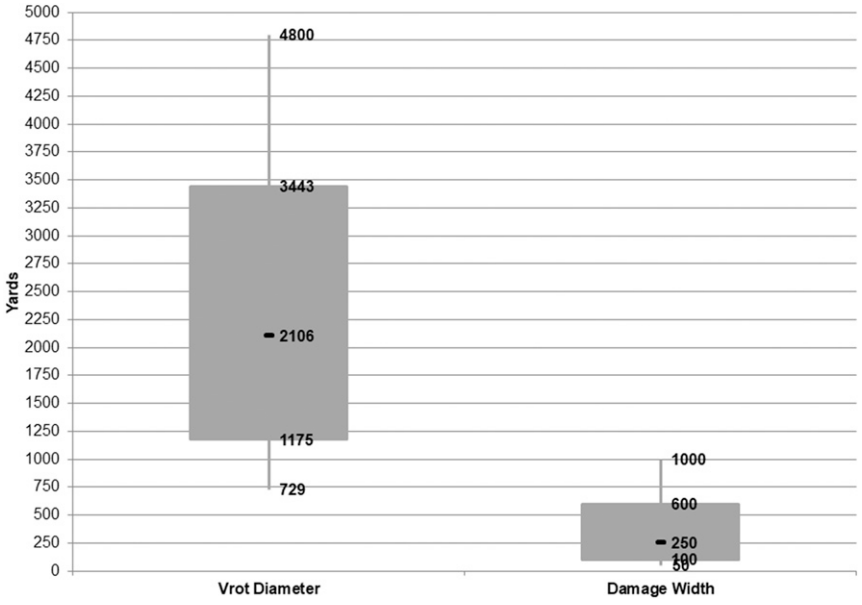

FIG. 2. Box-and-whisker plot of tornado damage path width (yards) vs the linear distance between the peak inbound and outbound WSR-88D velocity gates used to calculate V_{rot}. The shaded boxes enclose the interquartile range (25th–75th percentiles with the median value labeled), and the whiskers extend to the 90th and 10th percentiles. Total sample of 6715 unique combinations of individual DIs with both damage path width and V_{rot} scan height ≤ 10 000 ft ARL (1 yard = 0.91 m).

logical extension of the S15 and T17 work is an examination of the applicability of V_{rot} and EF-scale on a scan-by-scan basis.

Any application of WSR-88D data to real-time tornado intensity estimates requires tornado damage matched in time with individual radar scans since the EF-scale damage ratings are the only consistent means of estimating tornado intensity. After the EF scale (WSEC 2006) was implemented to assign wind-engineered intensity estimates to tornado damage in 2007, the Damage Assessment Toolkit (DAT; Camp et al. 2010) was created to digitally archive tornado damage metadata. The NWS began the DAT-based data collection effort in 2007 for a few select tornado events. A larger fraction of tornadoes was digitally archived in the DAT as this practice became increasingly adopted by more NWS local forecast offices in recent years.[2] The EF-scale contains 28 wind-engineered damage indicators (DIs), each categorized by degrees of damage (DoD) that indicate a range of possible wind speeds (WSEC 2006). Variability in tornado rating and associated wind speed can occur due to a multitude of factors including tornado surveyor experience, interpretation of the debris field, and availability of DIs (Edwards et al. 2013).

This study extends the work of LaDue et al. (2012) and Kingfield and LaDue (2015), who investigated WSR-88D mesocyclone and tornado detection algorithm output in comparison to finescale tornado survey data (i.e., DIs), by examining DIs in comparison to V_{rot} for a much larger sample of tornadoes [i.e. 179 individual WSR-88D scans in LaDue et al. (2012) versus 7513 individual scans in this work]. This work also considers explicit peak DI wind speed estimates in addition to the coarser EF-scale categories. The primary goal is to evaluate real-time probabilities of tornado intensity via V_{rot} and STP, conditioned on tornado occurrence.

2. Data and methods

a. Tornado path data

A record of tornado damage paths was derived from the "ONETOR" tornado dataset described by Schaefer and Edwards (1999). ONETOR stitches together the county-based

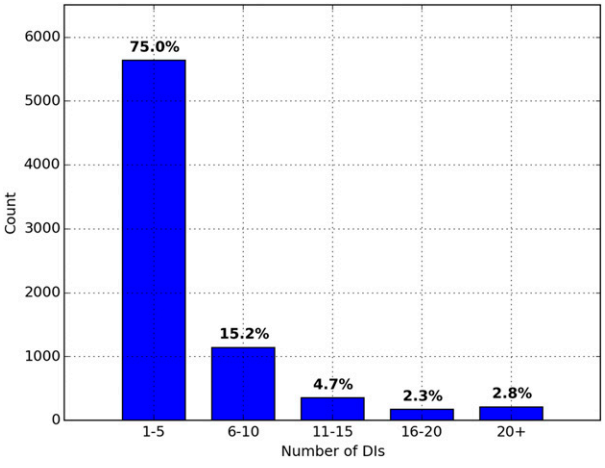

FIG. 3. Frequency of DIs by 0.5° DI scan (7513), binned every five DIs. Total sample of 38 758 DIs for 7513 DI scans.

[2] NWS field offices were mandated to list all tornadoes in the DAT in 2018, just after the 2009–17 study period.

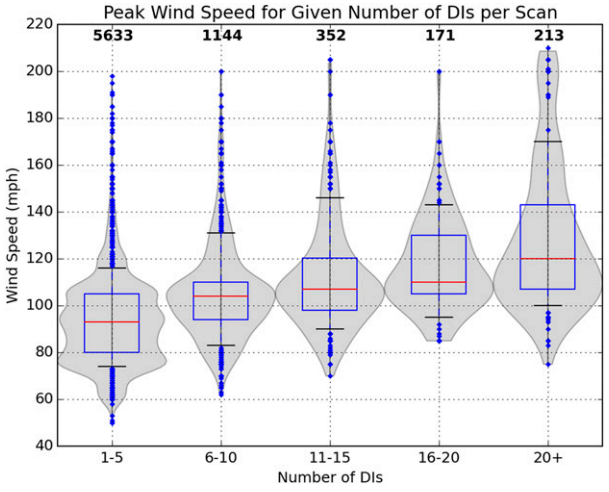

FIG. 4. Distributions of peak DI-estimated wind speed relative to the (aggregated/binned) number of DIs available for each WSR-88D volume scan analyzed in the 2009–17 dataset. Distributions are visualized using a combination of violin plots for the entire distribution (gray shading) and box-and-whisker plots, with the blue box indicating the interquartile range, the red line indicating the median, the whiskers indicating the 10th and 90th percentile values, and the blue dots indicating the outliers. The total count within each distribution is labeled at the top of each column. Total sample sizes are as in Fig. 3 (1 mph = 0.447 m s^{-1}).

tornado information from *Storm Data* into one tornado record. For example, a tornado spanning two counties is treated as just one tornado rather than two tornado segments. Each DI from the DAT dataset was associated manually with parent tornado data, resulting in over 43 000 initial DIs matched to nearly 3400 tornadoes from 2009 to 2017. Nonstandard DIs (i.e., 29 ''other'') were discarded in favor of wind-engineered estimates of wind speed (DIs 1–28).

A few well-surveyed tornadoes, not included in the DAT, were added manually to our tornado database. The authors reconstructed a sequence of DIs and peak wind speed estimates from storm surveys (e.g., the 2 March 2012, Henryville, Indiana, EF4 tornado), and an equivalent DAT was also reconstructed for the 22 May 2011 Joplin, Missouri, EF5 tornado from structure-by-structure EF-scale damage (Marshall et al. 2012).

b. V_{rot} procedure

Radar data were obtained from the National Centers for Environmental Information (http://www.ncdc.noaa.gov/nexradinv/) for each tornado with DIs from 2009 to 2017, which encompasses the era of ''super-resolution'' data (Brown et al. 2005; Torres and Curtis 2007). Level II data from the nearest WSR-88D site were examined via Gibson Ridge Level II radar-viewing software (http://www.grlevelx.com/), and V_{rot}, [defined as $(V_{max\_outbound} - V_{min\_inbound})/2$] was calculated manually as in S15 and T17, but for each WSR-88D 0.5° scan during the lifetime of each tornado. The center point of the line connecting the centroid of the maximum inbound and outbound velocity gates (Fig. 1) was used to match DIs to V_{rot} from the closest scan. The time interval of 0.5° scans varied depending on the WSR-88D scanning strategy. Higher temporal frequency of 0.5° scans from the supplemental adaptive intravolume low-level scan (SAILS; Chrisman 2011) and multiple elevation scan option for SAILS (MESO-SAILS, Chrisman 2014) strategies were implemented during the

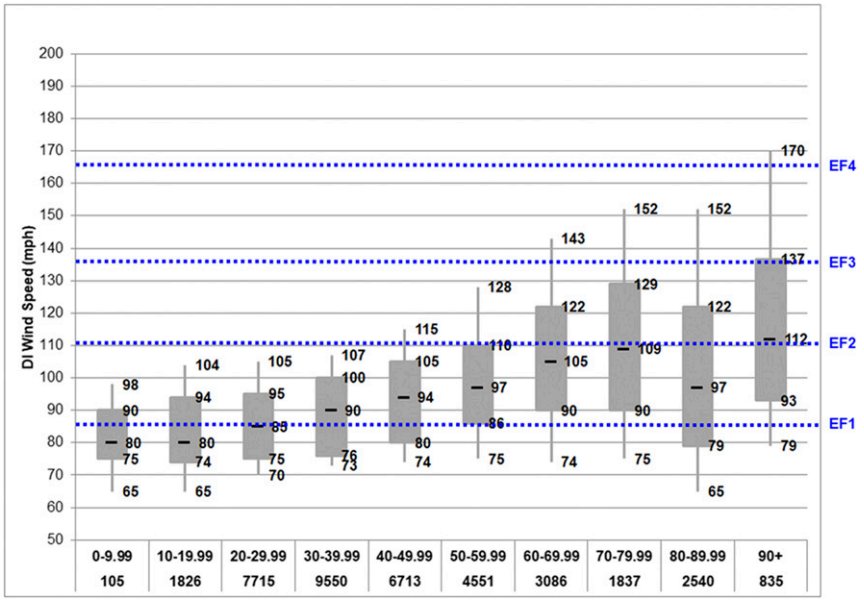

FIG. 5. Box-and-whisker plot of DI wind speeds (mph) by V_{rot} (kt), for 38 758 DIs (1–28) with accompanying V_{rot} scan height ≤ 10 000 ft ARL. The shaded boxes denote the interquartile range (25th–75th percentiles, with the median values marked), and the whiskers extend to the 10th and 90th percentiles. Total number of DIs in each V_{rot} bin are shown in the bottom row (1 mph = 0.447 m s^{-1}, 1 kt = 0.514 m s^{-1}).

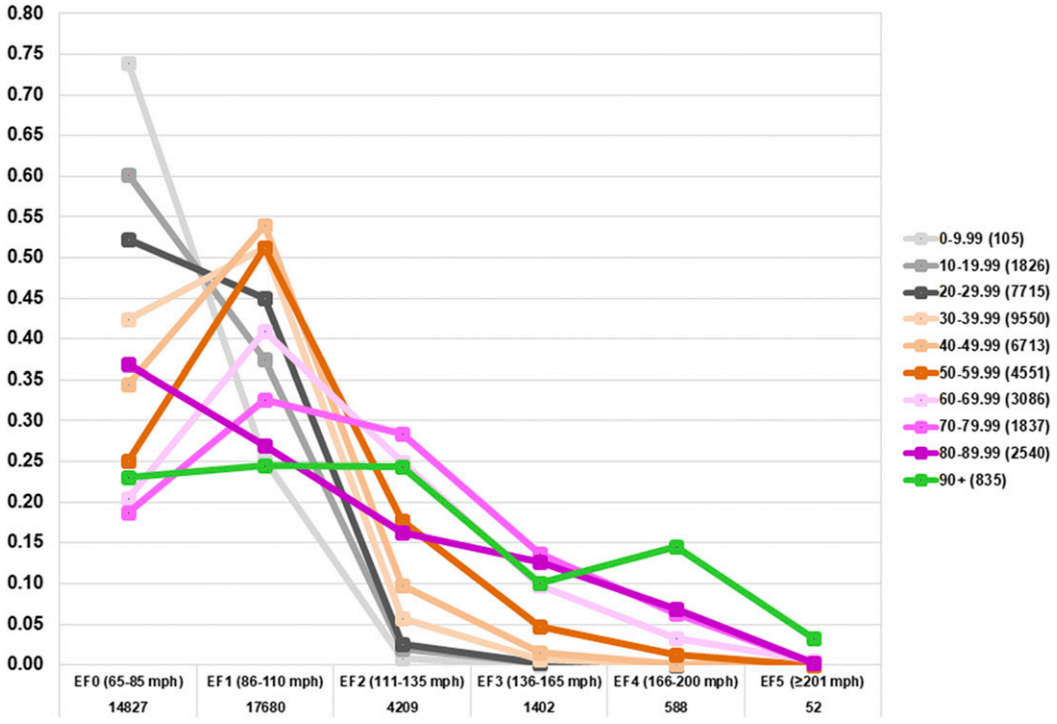

FIG. 6. Fraction of all surveyed DI wind speeds for each EF-scale category, binned by V_{rot} (every 10 kt; 1 mph = 0.447 m s^{-1}, 1 kt = 0.514 m s^{-1}). Total sample size of 38 758 individual DIs with accompanying V_{rot} scan height ≤ 10 000 ft ARL.

2009–17 study period. The 0.5° scan intervals decreased from 4 to 5 min to approximately every 2.5 and 1.5 min when utilizing SAILS or MESO-SAILS, respectively. This change in scan update frequency during our sample period adds some uncertainty to the DI matching with V_{rot} prior to MESO-SAILS, but we chose to use all available scans going back to 2009 to maximize the sample size of high-end (EF3+) damage.

A manually intensive process to record only velocity gates exhibiting characteristics of meteorological returns (i.e., reflectivity ≥ 20 dbZ; correlation coefficient ρ_{HV} ≥ 95%) was utilized to remove sidelobe (Piltz and Burgess 2009) contaminated velocity gates from consideration. Velocity maxima exhibiting cyclonic azimuthal shear within 5 n mi (9.26 km) and ≤45° angle from a line orthogonal to the beam were considered, to avoid primarily convergent or divergent signatures. If two distinct outbound (inbound) maxima gates for V_{rot} consideration were present in the two-dimensional velocity field, the inner outbound (inbound) gate's velocity was recorded. In rare cases where identification of V_{rot} remained difficult, velocity pairing was limited to within the ρ_{HV} reduction area from a polarimetric tornadic debris signature [TDS, when present; Ryzhkov et al. 2005; Schultz et al. 2012a; Bodine et al. 2013; Van Den Broeke and Jauernic 2014; Snyder and Ryzhkov 2015]. The ρ_{HV} reduction from tornadic debris can persist after tornado demise (Schultz et al. 2012b), but our data collection did not extend beyond the end of the surveyed tornado paths. In very rare cases when the 0.5° tilt contained aliased, range-folded, or contaminated velocity data (16 scans, or 0.2% of 7513 during the 2009–17 period), the 0.9° tilt was used as a supplemental tilt.

Each DI was manually assigned a convective mode using the definitions of Smith et al. (2012) for right-moving supercells (RM) and quasi-linear convective systems (QLCS; ≥3:1 aspect ratio of reflectivity ≥ 35 dbZ that is ≥100 km in length).

c. *Matching DIs to V_{rot}*

Initially, 43 000+ DIs were considered from 2009 to 2017. All nonstandard DIs, DIs missing accompanying radar data or near-storm environment data (see section 2d below), and scans with V_{rot} higher than 10 000 ft above radar level (ARL) were removed, leaving a sample of 38 758 DIs. The V_{rot} calculations necessarily represent broad, storm-scale rotation at instantaneous points along portions of each tornado path. Per Fig. 2, tornado damage path widths tend to be much narrower than the distance between maximum inbound and outbound velocity gates in the V_{rot} calculation, by roughly a factor of 5–15; also see Burgess et al. (2002). Moreover, the fastest tornado translation speeds [~50 kt (25 m s^{-1})] result in tornado movement of roughly 1.5 n mi (2.78 km) in the 1.5 min between MESO-SAILS scan updates, which is roughly equivalent to the 70th percentile of WSR-88D V_{rot} diameter (Fig. 2). Thus, the area covered by successive WSR-88D V_{rot} scans can overlap and high precision is not necessarily possible when mapping DIs to V_{rot}.

For a vast majority of WSR-88D 0.5° scans, five or fewer DIs were matched to a particular V_{rot} (Fig. 3), with large numbers

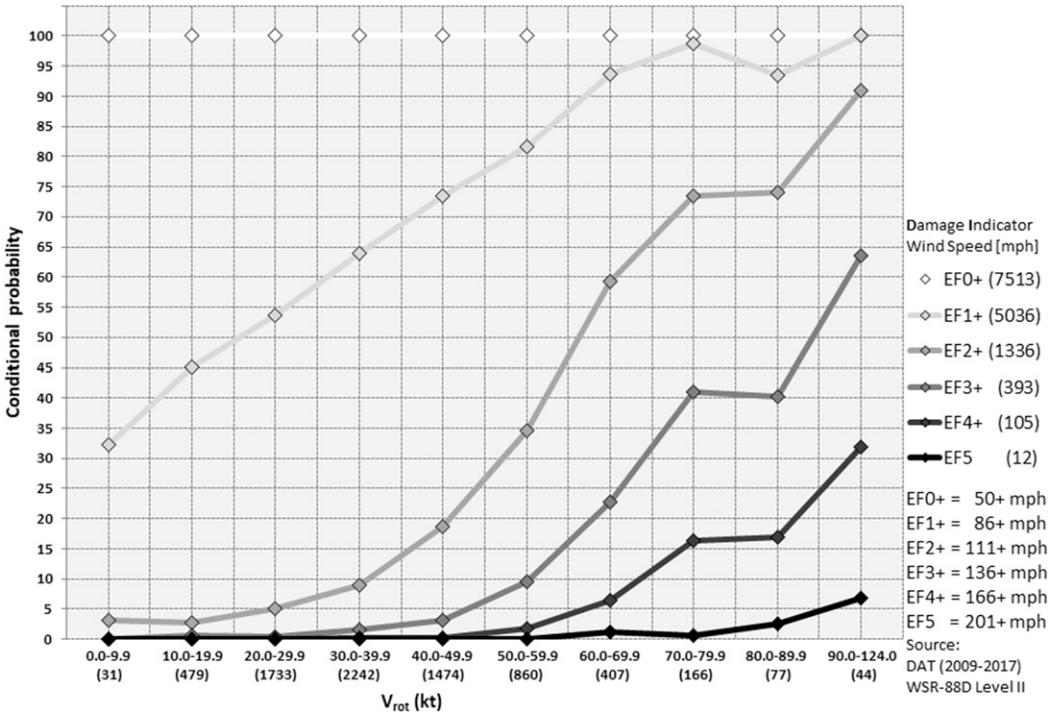

FIG. 7. Conditional probability of EF-scale exceedance (legend) for rotational velocity (V_{rot}) [kt; *x* coordinate, (sample size)] for all 7513 individual 0.5° scans for surveyed tornadoes [2009–17; ≤10 000 ft (3048 m) ARL, 1–101-mi (1.6–161 km) radius; 1 mph = 0.447 m s^{-1}, 1 kt = 0.514 m s^{-1}].

of DIs per scan (>20) limited to a few well-surveyed, high-end tornadoes in densely populated areas. Peak damage ratings and estimated peak wind speeds did tend to increase as the number of DIs increased for a given radar scan (Fig. 4). This signal is primarily a function of increasing population density with increasing numbers of DIs, which is related to the tendency for more intense tornadoes to have longer and wider paths (Brooks 2004). Yet, the vast majority of radar scans did not have a large number of accompanying DIs. The lack of explicit timing information from the DAT to individual DIs combined with relatively broad V_{rot} diameter did not allow precise matching of DIs in time to the radar scans (i.e., to within tens of seconds).

As expected, all V_{rot} ranges are associated with weaker DI wind speeds in the low end of the distributions (e.g., the 10th percentile values in Fig. 5). The signal for increasing DI wind speeds with increasing V_{rot} is most pronounced for the highest percentile rankings (e.g., the 90th percentile values in Fig. 5). Per Fig. 5, once V_{rot} values reach 50–59.9 kt (1 kt ≈ 0.51 m s^{-1}), the upper quartile of DI wind speed estimates exceed the minimum threshold for EF2 damage. Likewise, as V_{rot} values increase in the 70–79.9-kt range, roughly half of all DI wind speed estimates exceed the minimum threshold for EF2 damage. A different way of illustrating the frequency of DIs by EF-scale and V_{rot} is shown in Fig. 6. Specifically, EF0 (65–85 mph, 29–38 m s^{-1}) DIs were most common with the weakest V_{rot} (0.0–9.9 kt, 0.0–5.1 m s^{-1}), whereas EF4+ (≥166 mph, 74 m s^{-1}) DIs were most common with the strongest V_{rot} (90.0–124.0 kt; Fig. 6). Low-end DIs were more common than high-end DIs for even the largest V_{rot}, because the entire path of a tornado has the potential to reveal low-end damage. The extremely detailed tornado-damage survey from the 20 May 2013 Moore, Oklahoma, EF5 tornado clearly illustrates the prevalence of low-end DIs. Per Fig. 5, multiple scans for the 20 May 2013 Moore tornado were associated with large numbers of DIs for V_{rot} in the 80.0–89.9-kt range, which skewed the entire distribution downward toward lower DI wind speeds. The distribution of potential DIs is not known with high precision in real time, and the majority of surveyed DIs will not coincide with the most intense portions of a tornado at any given time. Given the aforementioned concerns in trying to precisely match DIs with radar scans and the limited number of DIs available for most scans, only the greatest DI was retained for each V_{rot}, which represents the S15 and T17 methodology applied to individual radar scans instead of the entire tornado path, which is effectively the *worst-case scenario* for each WSR-88D scan with *observed tornadoes*, as predicted speeds will frequently exceed many, if not all, survey point velocities for a variety of reasons.

NWS warning responsibilities extend to areas less well-covered by the NEXRAD network, so we compromised between increased radar resolution in the low levels at closer range and the NWS mission to protect lives and property, which includes areas with lesser WSR-88D coverage [i.e., 75–100 mi (121–161 km) and beyond the radar sites]. Thus, radar scans with both velocity gates ≤ 10 000 ft (3048 m) height ARL

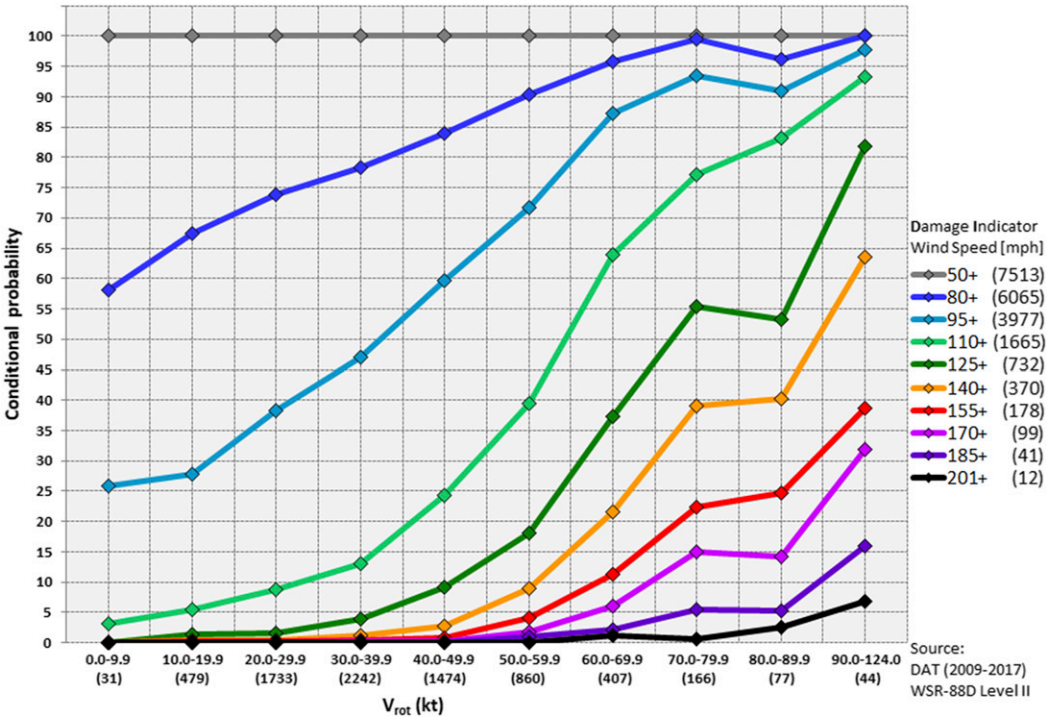

FIG. 8. As in Fig. 7, but for peak DI wind speed exceedance (mph; 1 mph = 0.447 m s^{-1}, 1 kt = 0.514 m s^{-1}).

[within ≤101 mi (163 km) of a radar site] were included in this study, consistent with the prior work by S15 and T17.

Despite WSR-88D radars not explicitly resolving tornadoes, Toth et al. (2013) showed that WSR-88D data vary in tandem with higher-resolution, mobile Doppler radar observations of tornadoes, albeit with lower V_{rot} for the WSR-88D data. Considering the breadth of recent work showing increases in WSR-88D V_{rot} as tornado damage intensity increases (e.g., LaDue et al. 2012; S15; Gibbs 2016; T17), it appears reasonable to use WSR-88D data in real time to estimate tornado intensity. Such use of WSR-88D data to estimate tornado intensity in real time relies on high-confidence, corroborating evidence that a tornado is ongoing (trustworthy spotter reports or a TDS).

d. *Matching DIs to the near-storm environment*

There are numerous ways to characterize the near-storm environment, ranging from subjective assessments of high-resolution satellite imagery and surface observations to observed soundings in proximity to a storm event. Past work with observed soundings considered rather broad proximity criteria and large sample sizes (e.g., Rasmussen and Blanchard 1998; Craven and Brooks 2004). Proximity soundings have also been derived from short-term model analyses, such as the real-time, hourly objective analysis fields produced by SPC since the early 2000s (Bothwell et al. 2002), based on 1-h forecast soundings from the Rapid Update Cycle (RUC; Benjamin et al. 2004). Model-based soundings within 40 km and 1 h of supercells were found to be representative of standard observations in regional storm environments (e.g., Thompson et al. 2003), and within the "Goldilocks Zone" for proximity soundings identified by Potvin et al. (2010). Special field project soundings have also been evaluated against the SPC mesoanalysis fields by Coniglio (2012), who found that the SPC mesoanalysis process reduces errors compared to the unaltered 1-h forecast soundings. Still, variability exists on the storm-scale that may not be reflected in the hourly analyses (Parker 2014). Overall, the aforementioned work confirms that the SPC mesoanalysis fields generated hourly at 40-km grid spacing are a reasonable representation of the near-storm environment, without the problem of contamination by storm-scale processes.

The date/time and location of the V_{rot} couplet centroids were matched to the closest grid point of archived SPC mesoanalysis data (Dean et al. 2006) for the hour immediately preceding the V_{rot} scan. The archived mesoanalysis data were based on the 0-h RUC model output adjusted for a two-pass Barnes scheme of surface observations from 2009 to April 2012, and the 0-h Rapid Refresh (RAP; Benjamin et al. 2016) model output from May 2012 to 2017. To reflect the potential for variability in the mesoscale environment, the maximum STP value within 80 km of each grid point (STP80km) was also calculated. After the combined filtering procedure (mentioned in section 2c) to remove nonstandard DIs, scans above 10 000 ft ARL, and missing mesoanalysis grid-hour data, 38 758 DIs and 7513 0.5° DI scans were retained for further analysis.

e. *Conditional tornado probabilities*

Conditional (i.e., upon the occurrence of a tornado) probabilities of tornado intensity, as measured by EF-scale damage, were calculated based on V_{rot}. Like in S15, V_{rot} was distributed

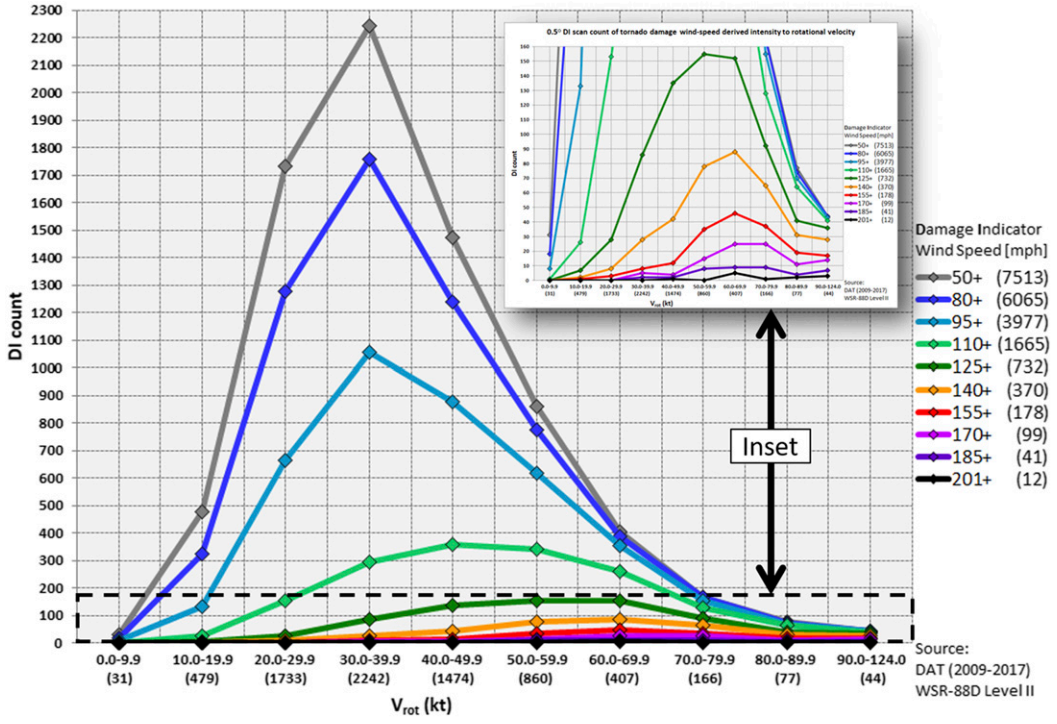

FIG. 9. Counts of peak DI wind speed exceedance by binned magnitudes of V_{rot} (kt, x coordinate). The inset shows the distributions of a zoomed subset of peak DI wind speeds (1 mph = 0.447 m s^{-1}, 1 kt = 0.514 m s^{-1}).

across a large range [i.e., 0–124 kt (0–63.8 m s^{-1})] and placed within 10-kt bins [e.g., 40.0–49.9 kt (20.6–25.7 m s^{-1})] due to limited sample sizes for specific V_{rot} values. The STP was examined in addition to V_{rot} in order to quantify the influence of near-storm environment on conditional tornado intensity probabilities. The nearest STP gridpoint value on the 40-km grid (i.e., STPgrid) and a neighborhood maximum value within a radius of 80 km (i.e., STP80km) were likewise binned into ranges of STP (e.g., 4.00–6.99) to calculate conditional tornado intensity probabilities.

3. Results and discussion

a. Variations in tornado intensity as a function of V_{rot}

A strong relationship between the hourly peak value of V_{rot} anywhere along the path of a tornado and EF rating was demonstrated in S15 (their Fig. 12). Accordingly, V_{rot} for DIs along a tornado path exhibited a similar overall signal of increasing conditional EF-scale exceedance probabilities as V_{rot} increased, on a scan-by-scan basis (Fig. 7). Relatively large differences in conditional tornado probabilities (34%) exist within some of the V_{rot} bins between the EF-scale categories [e.g., EF1+ versus EF2+ for V_{rot} = 60.0–69.9 kt (30.9–36.0 m s^{-1})]. Figure 7 includes SAILS and MESO-SAILS scans (updated every ~2.5 to 1.5 min, respectively), though the EF-scale exceedance probabilities remain consistent with prior work by S15 (their Fig. 12) using a legacy scan update frequency of once every ~4.5 min.

Past attempts to discriminate tornado intensity via damage ratings have relied on relatively large wind speed ranges (e.g., S15 and others) inherent to the EF-scale. EF-scale ratings are associated with wind speed ranges [e.g., EF0, 65–85 mph (29–38 m s^{-1})] whereas the DAT contains wind speed data in 1-mph (0.447 m s^{-1}) increments. The more precise wind speeds in the DAT afford an opportunity to develop conditional probabilities with more wind speed thresholds than the EF0–EF5 ranges alone (e.g., wind speed exceedance probabilities in Fig. 8).

A majority of V_{rot} values (73%) fell in the range of 20.0–49.9 kt (10.3–25.7 m s^{-1}; Fig. 9). This range of V_{rot} with tornadoes largely overlaps values associated with severe, nontornadic supercells and QLCS (T17; their Fig. 8), with correspondingly low tornado probabilities. Consequently, it will continue to prove difficult to discern between tornadic and nontornadic storms on a scan-by-scan basis for weaker V_{rot} [i.e., ≤49.9 kt (25.7 m s^{-1})], hence the need for additional confirmation of an ongoing tornado.

As V_{rot} increases, the conditional probabilities of DI wind speed-exceedance estimates increase (Fig. 8). The increase is most pronounced for 95+ mph (42+ m s^{-1}) and greater wind speed-exceedance estimates, as V_{rot} increases from 40.0–49.9 kt (20.6–25.7 m s^{-1}) to 70.0–79.9 kt (36.0–41.1 m s^{-1}). The increase in V_{rot} through this range corresponds to 1) the transition of tornado probabilities from <50% to ~100% (T17), and 2) some of the largest probability changes for different wind speed-exceedance thresholds [Fig. 8, (e.g., 110+ mph, 49+ m s^{-1})]. Given the strong relationship between maximum

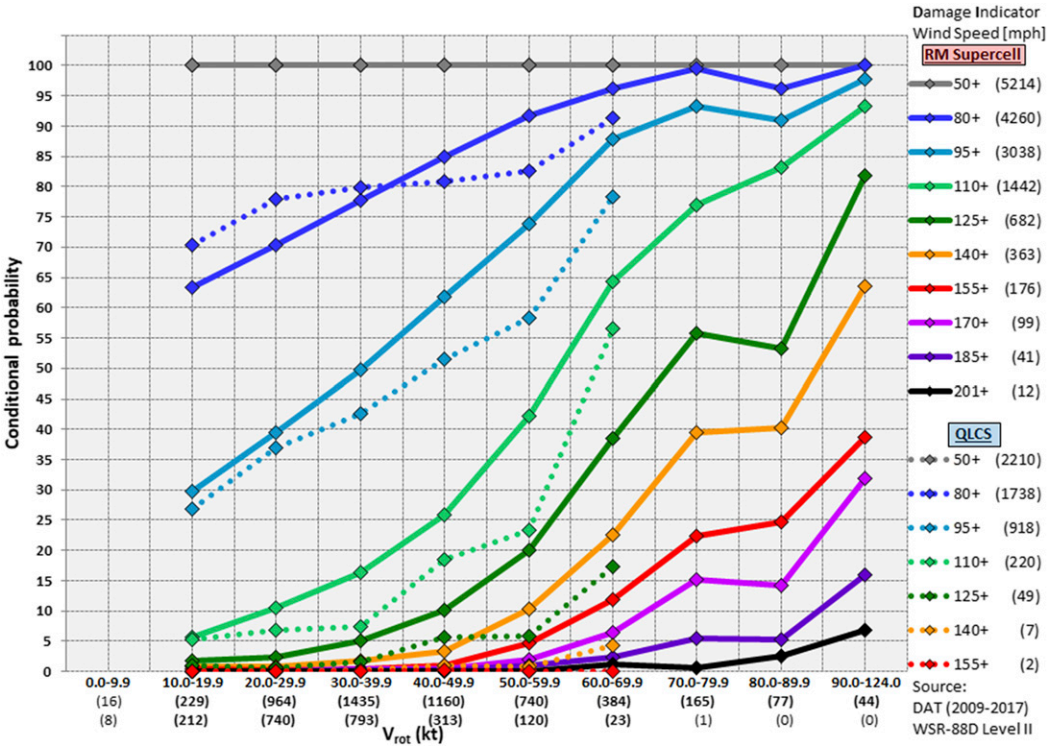

FIG. 10. As in Fig. 8, but for right-moving supercells (RM) and QLCS. Data are only plotted within V_{rot} bins containing ≥20 cases (1 mph = 0.447 m s^{-1}, 1 kt = 0.514 m s^{-1}).

DI wind speed and V_{rot}, increases in V_{rot} can be used to heighten awareness of increasing tornado potential and potential damage intensity.

Convective mode was also documented with each V_{rot} scan and almost all tornadic storms (with accompanying DIs) were classified as either RM (70.5%) or QLCS (28.4%). Though probabilities with QLCSs were 5%–10% lower than RM for the same peak DI wind speeds, there appears to be little practical difference evident in V_{rot} between the two storm types (Fig. 10) for $V_{rot} < 50$ kt (25.7 m s^{-1}). It is unknown whether the small differences between RM and QLCS are attributable to radar sampling or sample-size limitations.

Following T17, V_{rot} scans were examined by height ARL in three groups [rounded to the nearest 100 ft (30 m) ARL]: 100–2900 ft (30–884 m), 3000–5900 ft (914–1798 m), and 6000–10 000 ft (1829–3048 m). Likewise, circulation diameter (measured by the distance between the centers of the velocity gates used for the V_{rot} calculation) was binned into three groups [i.e., 0.00–0.99 n mi (0.00–1.84 km), 1.00–1.99 n mi (1.85–3.69 km), and 2.00–5.00 n mi (3.70–9.26 km)]. No practical differences were noted between the binned values of height ARL and resultant DI wind speed probabilities (not shown). Similar to the findings of T17, the greatest peak DI wind speed probabilities were for V_{rot} scans close to the radar [i.e., 100–2900 ft (30–884 m) ARL] and with small circulation diameters [<1 n mi (1.85 km); Fig. 11]. Thus, confidence in peak DI wind speed estimates is greatest when tornadic storms are sampled close to the ground and near the radar, as opposed to broad circulations sampled at large distances (high height ARL) from the radar. A denser radar network in tornado prone areas east of the Rockies (Smith et al. 2012, their Fig. 8c) would likely lead to improvements in discerning tornado intensity where "gaps" in low-level radar coverage currently exist. Even with suboptimal radar coverage for a particular tornado, emphasis must still be placed on skillful interpretation of velocity data to provide the most meteorologically sound, real-time estimates of tornado damage potential.

The variation of the conditional probabilities can be demonstrated (Fig. 8) by examining varying probability for different wind speed-exceedance thresholds as a function of V_{rot} and vice versa. For example, a 68.5-kt (35.2 m s^{-1}) V_{rot} (e.g., 0204 UTC data in Fig. 1) yields a 64% and 11% conditional tornado probability for 110+ mph (49+ m s^{-1}) and 155+ mph (69+ m s^{-1}) damage, respectively. Using that same 45 mph difference in peak DI wind speed exceedance, but for stronger DI wind speeds (i.e., 140+ mph versus 185+ mph) in the same range of V_{rot} (the 60s), the probability differences are only ~20%, and the tornado probabilities are low (~22% and 2%, respectively). The differences in exceedance probabilities for the 140+ and 185+ mph peak DI wind speeds become larger (~35%–50%) on the high end of the V_{rot} spectrum (i.e., ≥70 kt), and the overall probabilities of high-end DI wind speeds also increase. Alternatively, a V_{rot} increasing from 38 kt (19.5 m s^{-1}) to 65 kt (33.4 m s^{-1}) results in 110+ mph (49+ m s^{-1}) probabilities increasing from 13% to 64%. Operational application could involve identification of critical wind speed-exceedance

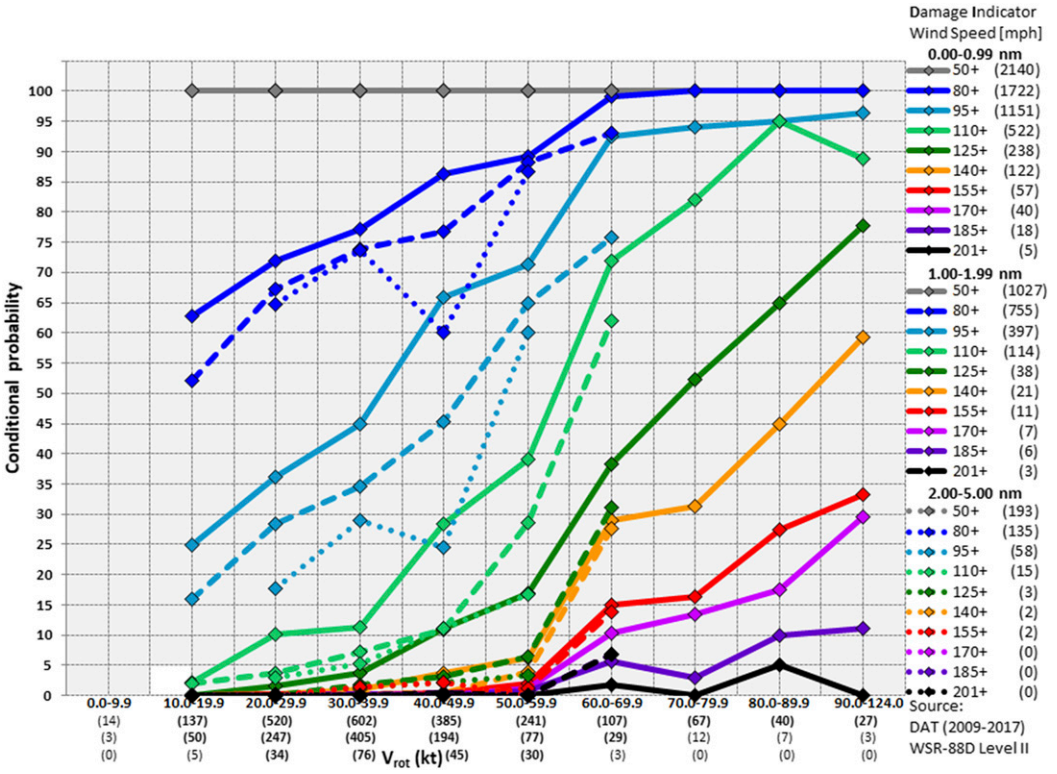

FIG. 11. As in Fig. 8, but for 100–2900 ft (30–884 m) ARL events by circulation diameter [0.00–0.99 n mi (0–1833 m), 1.00–1.99 n mi (1834–3703 m), and 2.00–5.00 n mi (3704–9260 m)]. Sample sizes are shown in parentheses by EF-scale rating (shown at right) and by V_{rot} bin. Data are only plotted within bins containing ≥20 cases (1 mph = 0.447 m s^{-1}, 1 kt = 0.514 m s^{-1}).

thresholds [e.g., >25% of 170+ mph (76+ m s^{-1})]. Although using probabilities of tornado-damage intensity may provide quantitative value based on V_{rot} alone (i.e., Figs. 7, 8, 10, 11), the near-storm environment can enhance or reduce the probabilities of a particular peak DI wind speed.

b. *Variations in tornado intensity as a function of near-storm environment*

A relatively simple characterization of the near-storm environment comes in the form of STP, which has been demonstrated to discriminate between significantly tornadic supercells and other severe storm environments (Thompson et al. 2003, 2012). Both STPgrid and STP80km indicate higher conditional tornadic wind speed probabilities as STP increases. For example, as STP80km increases from 1.5 to 8, the 110+ mph (49+ m s^{-1}) conditional probability more than triples from 13% to 41% (Fig. 12). Alternatively, the same increase in STP80km (i.e., from 1.5 to 8) results in a change from 13% conditional probability of 110+ mph (49+ m s^{-1}) damage to a 14% conditional probability of 140+ mph (63+ m s^{-1}) damage. As shown by both S15 and T17, inclusion of STP can result in improved discrimination between weaker and stronger tornadoes, though only limited discrimination is possible when comparing values in adjacent bins in Fig. 12. The near-storm environment contributes to greater confidence in tornado intensity differences when comparing situations with larger differences across multiple bins (e.g., probabilities of an EF2+ tornado roughly double as STP80km increases from <1 to 3–4, or from 3–4 to ≥10.

c. *Estimating tornado intensity from a combination V_{rot} and STP*

As documented in the prior sections and in prior work by S15 and T17, V_{rot} and STP80km serve as proxies for tornado intensity and the near-storm environment, respectively, where expected tornado intensity increases as both V_{rot} and STP80km increase. Conditional peak DI wind speed probabilities were developed based on binned ranges of V_{rot} and STP80km. Conditional probabilities for 80+ mph (36+ m s^{-1}) 0.5° DI scans increased as a function of both increasing V_{rot} and increasing STP80km (Fig. 13a). Similar trends at lower conditional probabilities are evident for 95+ mph (42+ m s^{-1}), 110+ mph (49+ m s^{-1}), and 125+ mph (56+ m s^{-1}), respectively (Figs. 13b–d). They increase substantially (by 25%–40%) as V_{rot} increases from 20 kt (10.3 m s^{-1}) to 70 kt (36 m s^{-1}) through much of the range of STP80km values. The V_{rot} exhibits a stronger influence on peak DI wind speed probabilities, though a lesser increase in conditional probabilities occurs as STP80km increases in the same bin of V_{rot}. Comparing to a similar analysis by S15 (their Fig. 14),

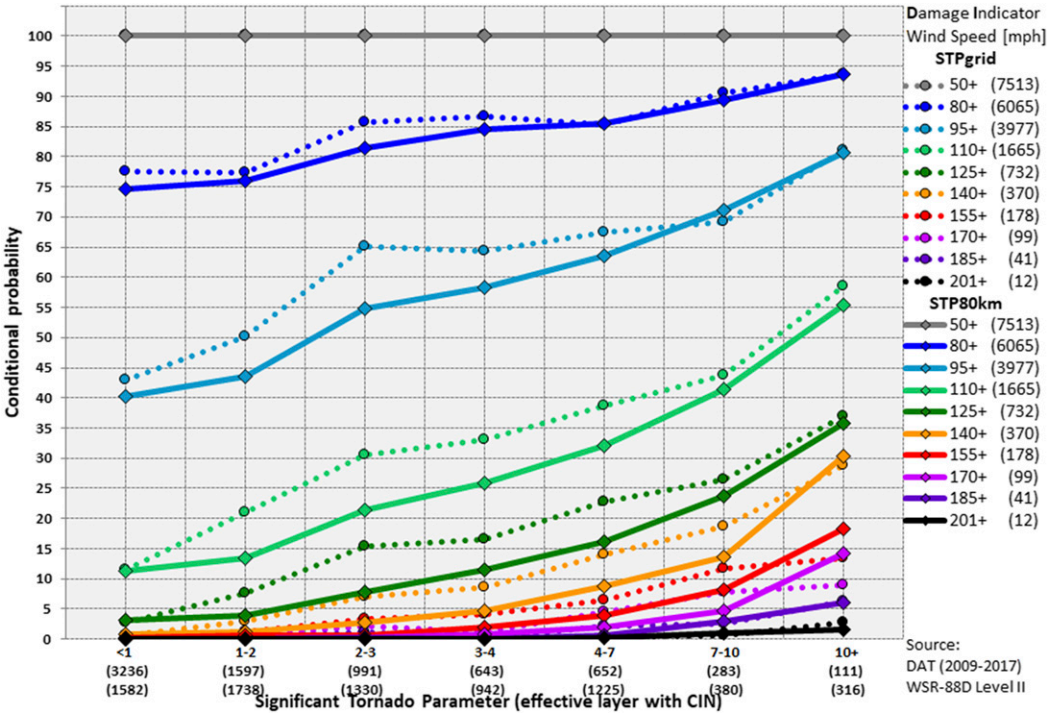

FIG. 12. As in Fig. 10, but for STPgrid vs STP80km maximum value (dimensionless, x coordinate; 1 mph = 0.447 m s^{-1}).

EF2+ conditional probabilities (Fig. 14) from this sample are 10%–20% lower for V_{rot} in the 40–70-kt (20.6–30.0 m s^{-1}) range. The lower probabilities in this study are likely the result of spatiotemporal matching of peak DIs to corresponding individual V_{rot} scans, as compared to more general matching of peak V_{rot} to peak damage anywhere during the lifetime of a tornado (i.e., the peak V_{rot} did not necessarily match the time/location of the peak damage). The conditional probabilities in Figs. 13 and 14 reflect the distribution of individual V_{rot} scans and peak DIs across the United States from 2009 to 2017 and do not necessarily apply equally to areas of very low (rural) and very high (urban) density of DIs.

4. Summary

An initial sample of nearly 43 000+ DIs from the DAT were matched to nearly 3400 tornadoes from the ONETOR database. The DIs were matched manually to the nearest radar signatures (i.e., V_{rot}) through examination of single-site WSR-88D level II data. After filtering out nonstandard DIs, cases with $V_{rot} > 10\,000$ ft ARL, or missing mesoanalysis grid-hour data, 38 758 individual DIs and 7513 0.5° elevation scans were retained. Distributions of DIs were examined as a function of V_{rot} and by the number of DIs per radar scan. Low-end DIs dominated the distributions across all ranges of V_{rot}, which is not surprising since the majority of tornado paths do not contain the most intense winds and/or damage. Ultimately, 7513 peak DIs were matched to V_{rot} scans in an attempt to emphasize potential peak tornado wind.

The prescribed V_{rot} approach to estimating peak damage potential, in combination with mesoscale environmental parameters, cannot resolve precise (down to the scale of seconds and meters) spatiotemporal variations in tornado intensity and resultant potential damage swaths. Low-end damage (EF0) is possible throughout a tornado path by definition, which makes low-end tornado damage ubiquitous. Tornadoes affecting more heavily populated areas are more likely to produce more intense DIs (all else being equal), which does increase the probability that damage could be overestimated in heavily populated areas. However, we are unaware of direct evidence suggesting systematic bias in tornado damage ratings that are the result of large numbers of DIs versus only small numbers of DIs. Thus, we advocate estimating potential peak tornado damage and/or wind speeds to be consistent with historical methods of rating and categorizing tornado damage (i.e., the common practice of referring to tornadoes by their maximum EF-scale rating). Any attempts to provide estimates of damage swaths and resultant damage distributions will require either more consistent/precise radar data (i.e., mobile Doppler radar observations at close range), or application of conceptual tornado vortex models in combination with widely available WSR-88D data, and thus our approach is effectively the worst-case scenario for each 88D scan as predicted speeds will frequently exceed many, if not all, survey point velocities for a variety of reasons.

This study demonstrates that more resolution in peak tornado wind speed (and resultant damage potential) are possible using peak DI wind speed-exceedance estimates instead of the

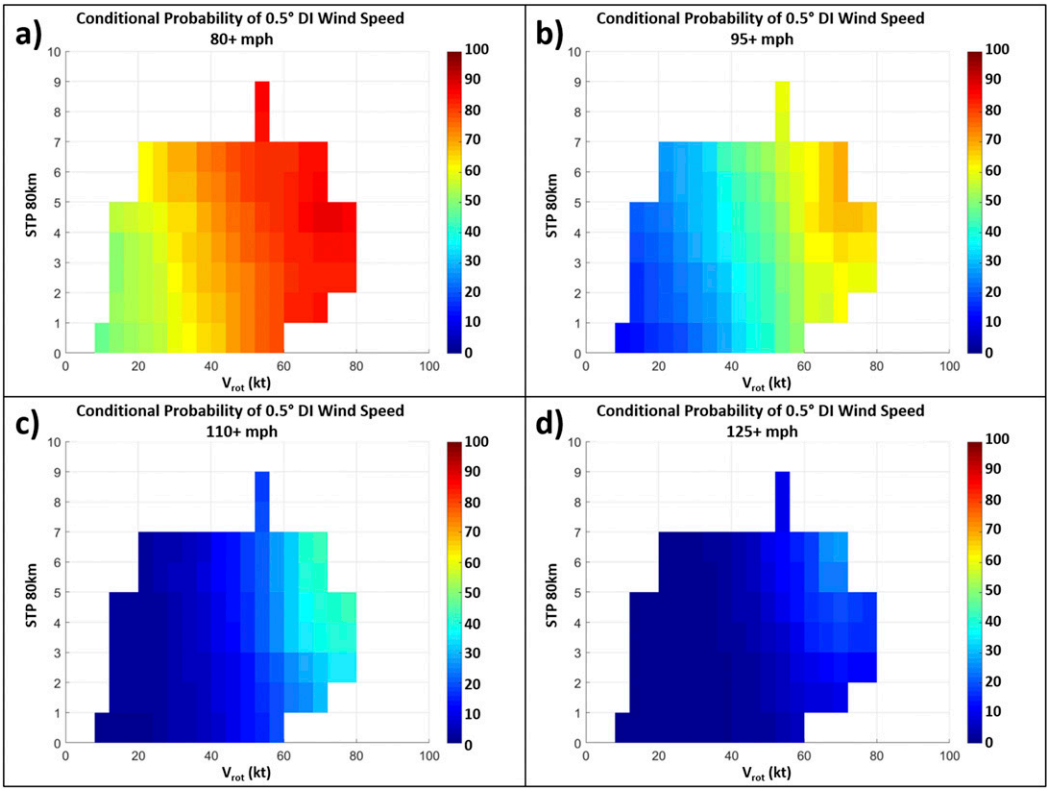

FIG. 13. Conditional probability of 0.5° DI scan wind speed (mph) by comparing 0.5° tilt angle V_{rot} (kt, x coordinate) vs STP80km (dimensionless, y coordinate) for (a) 80+, (b) 95+, (c) 110+, and (d) 125+ mph (1 mph = 0.447 m s^{-1}, 1 kt = 0.514 m s^{-1}).

coarser EF-scale ranges of peak DI wind speeds. Conditional probabilities for peak DI wind speed exceedance increase (decrease) as both V_{rot} and STP increase (decrease). Confident discrimination of potential tornado intensities with STP relies on relatively large differences in near-storm environment (see Fig. 12), while more common (small) differences are unlikely to provide much discrimination between weak (EF0–1) and significant (EF2+) tornadoes. More confident discrimination is possible with V_{rot}, especially for smaller diameter velocity couplets (say, <1 n mi diameter) sampled relatively close to the radar sites (see Fig. 11, as well as Figs. 9 and 10 from T17), as well as the tendency for stronger tornadoes to produce a TDS (T17; their Fig. 11).

Tornado warning decisions with appropriate lead time require more complex approaches involving full-volumetric assessment of storm structure, changes over time, and comparisons to expectations based on the near-storm environment and convective mode. Gibbs and Bowers (2019) suggest using a combination of rotational speed (a function of V_{rot} strength and diameter) and mesocyclone depth several volume scans (~10–20 min) prior to tornadogenesis, to provide lead time on tornado warnings for significant (EF2+) tornadoes. However, Gibbs and Bowers (2019) did not consider tornado intensity variations beyond the onset of EF2+ damage. An information gap still exists within the context of tornado warnings that can be addressed by V_{rot} derived from WSR-88D data, which enables *diagnostic* estimates of peak damage potential in real time that are consistent with how tornadoes have been characterized historically (i.e., maximum EF-scale damage ratings). Real-time estimates of tornado intensity with WSR-88D data and near-storm environment, can

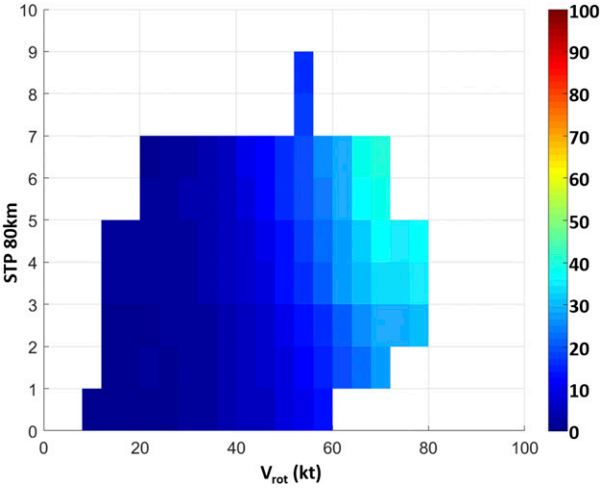

FIG. 14. As in Fig. 13, but for EF2+ (111+ mph; 1 mph = 0.447 m s^{-1}, 1 kt = 0.514 m s^{-1}).

help guide or reinforce warning decisions and emergency response efforts in the immediate aftermath of damaging tornadoes, with the caveat that direct evidence of tornado occurrence is available (i.e., high-confidence spotter reports or a TDS).

Acknowledgments. This manuscript was improved thanks to a rigorous review and thoughtful comments provided by Dr. Matthew Bunkers (NWS Rapid City), three anonymous reviewers, and Dr. Israel Jirak and Jeremy Grams (SPC). The authors thank Matt Mosier (SPC) for his assistance with Figs. 2 and 5. This study benefitted from discussions with Dr. Israel Jirak and William Bunting (SPC), Todd Lindley and David Andra (NWS Norman), and Dr. Harold Brooks (NSSL). Thanks to Parks Camp (NWS Tallahassee) for providing DAT data and Timothy Marshall for providing tornado survey information from the 22 May 2011 Joplin, Missouri, tornado.

REFERENCES

Benjamin, S. G., and Coauthors, 2004: An hourly assimilation–forecast cycle: The RUC. *Mon. Wea. Rev.*, **132**, 495–518, https://doi.org/10.1175/1520-0493(2004)132<0495:AHACTR>2.0.CO;2.

——, and Coauthors, 2016: A North American hourly assimilation and model forecast cycle: The Rapid Refresh. *Mon. Wea. Rev.*, **144**, 1669–1694, https://doi.org/10.1175/MWR-D-15-0242.1.

Bluestein, H. B., K. J. Thiem, J. C. Snyder, and J. B. Houser, 2018: The multiple-vortex structure of the El Reno, Oklahoma, tornado on 31 May 2013. *Mon. Wea. Rev.*, **146**, 2483–2502, https://doi.org/10.1175/MWR-D-18-0073.1.

——, ——, ——, and ——, 2019: Tornadogenesis and early tornado evolution in the El Reno, Oklahoma, supercell on 31 May 2013. *Mon. Wea. Rev.*, **147**, 2045–2066, https://doi.org/10.1175/MWR-D-18-0338.1.

Bodine, D. J., M. R. Kumjian, R. D. Palmer, P. L. Heinselman, and A. V. Ryzhkov, 2013: Tornado damage estimation using polarimetric radar. *Wea. Forecasting*, **28**, 139–158, https://doi.org/10.1175/WAF-D-11-00158.1.

Bothwell, P. D., J. A. Hart, and R. L. Thompson, 2002: An integrated three-dimensional objective analysis scheme in use at the Storm Prediction Center. Preprints, *21st Conf. on Severe Local Storms*, San Antonio, TX, Amer. Meteor. Soc., JP3.1, https://ams.confex.com/ams/pdfpapers/47482.pdf.

Brooks, H. E., 2004: On the relationship of tornado path length and width to intensity. *Wea. Forecasting*, **19**, 310–319, https://doi.org/10.1175/1520-0434(2004)019<0310:OTROTP>2.0.CO;2.

Brown, R. A., and L. R. Lemon, 1976: Single Doppler radar vortex recognition. Part II: Tornadic vortex signatures. Preprints, *17th Conf. on Radar Meteorology*, Seattle, WA, Amer. Meteor. Soc., 104–109.

——, ——, and D. W. Burgess, 1978: Tornado detection by pulsed Doppler radar. *Mon. Wea. Rev.*, **106**, 29–38, https://doi.org/10.1175/1520-0493(1978)106<0029:TDBPDR>2.0.CO;2.

——, B. A. Flickinger, E. Forren, D. M. Schultz, D. Sirmans, P. L. Spencer, V. T. Wood, and C. L. Ziegler, 2005: Improved detection of severe storms using experimental fine-resolution WSR-88D measurements. *Wea. Forecasting*, **20**, 3–14, https://doi.org/10.1175/WAF-832.1.

Burgess, D. W., R. J. Donaldson Jr., and P. R. Desrochers, 1993: Tornado detection and warning by radar. *The Tornado: Its Structure, Dynamics, Prediction, and Hazards*, *Geophys. Monogr.*, Vol. 79, Amer. Geophys. Union, 203–221.

——, M. A. Magsig, J. Wurman, D. C. Dowell, and Y. Richardson, 2002: Radar observations of the 3 May 1999 Oklahoma City tornado. *Wea. Forecasting*, **17**, 456–471, https://doi.org/10.1175/1520-0434(2002)017<0456:ROOTMO>2.0.CO;2.

Camp, P. J., K. Stellman, and J. Settelmaier, 2010: Utilizing mobile devices for enhanced storm damage surveys. *26th Conf. on Interactive Information and Processing Systems (IIPS) for Meteorology, Oceanography, and Hydrology*, Atlanta, GA, Amer. Meteor. Soc., 5B.4, https://ams.confex.com/ams/90annual/techprogram/paper_161540.htm.

Chrisman, J. N., 2011: Supplemental adaptive intra-volume low-level scan (SAILS). NOAA, 13 pp., http://www.roc.noaa.gov/wsr88d/PublicDocs/NewTechnology/SAILS_Initial_Presentation_Sep_2011.pdf.

——, 2014: Multiple elevation scan option for SAILS (MESO-SAILS). NOAA, 27 pp., http://www.roc.noaa.gov/wsr88d/PublicDocs/NewTechnology/MESO-SAILS_Description_Briefing_Jan_2014.pdf.

Coniglio, M. C., 2012: Verification of RUC 0–1-h forecasts and SPC mesoscale analyses using VORTEX2 soundings. *Wea. Forecasting*, **27**, 667–683, https://doi.org/10.1175/WAF-D-11-00096.1.

Craven, J. P., and H. E. Brooks, 2004: Baseline climatology of sounding derived parameters associated with deep moist convection. *Natl. Wea. Dig.*, **28**, 13–24.

Dean, A. R., R. S. Schneider, and J. T. Schaefer, 2006: Development of a comprehensive severe weather forecast verification system at the Storm Prediction Center. *23rd Conf. on Severe Local Storms*, St. Louis, MO, Amer. Meteor. Soc., P2.3, https://ams.confex.com/ams/23SLS/techprogram/paper_115250.htm.

Edwards, R., J. G. LaDue, J. T. Ferree, K. Scharfenberg, C. Maier, and W. L. Coulbourne, 2013: Tornado intensity estimation: Past, present, and future. *Bull. Amer. Meteor. Soc.*, **94**, 641–653, https://doi.org/10.1175/BAMS-D-11-00006.1.

French, M. M., H. B. Bluestein, I. PopStefanija, C. A. Baldi, and R. T. Bluth, 2013: Reexamining the vertical development of tornadic vortex signatures in supercells. *Mon. Wea. Rev.*, **141**, 4576–4601, https://doi.org/10.1175/MWR-D-12-00315.1.

——, ——, ——, ——, and ——, 2014: Mobile, phased-array, Doppler radar observations of tornadoes at X band. *Mon. Wea. Rev.*, **142**, 1010–1036, https://doi.org/10.1175/MWR-D-13-00101.1.

Gibbs, J. G., 2016: A skill assessment of techniques for real-time diagnosis and short-term prediction of tornado intensity using the WSR-88D. *J. Oper. Meteor.*, **4**, 170–181, https://doi.org/10.15191/nwajom.2016.0413.

——, and B. R. Bowers, 2019: Techniques and thresholds of significance for using WSR-88D velocity data to anticipate significant tornadoes. *J. Oper. Meteor.*, **7**, 117–137, https://doi.org/10.15191/nwajom.2019.0709.

Kingfield, D. M., and J. G. LaDue, 2015: The relationship between automated low-level velocity calculations from the WSR-88D and maximum tornado intensity determined from damage surveys. *Wea. Forecasting*, **30**, 1125–1139, https://doi.org/10.1175/WAF-D-14-00096.1.

LaDue, J. G., K. L. Ortega, B. R. Smith, G. J. Stumpf, and D. M. Kingfield, 2012: A comparison of high resolution tornado surveys to Doppler radar observed vortex parameters: 2011–2012 case studies. *26th Conf. on Severe Local Storms*, Nashville, TN, Amer. Meteor. Soc., 6.3, https://ams.confex.com/ams/26SLS/webprogram/Paper212627.html.

Marquis, J., Y. Richardson, P. Markowski, J. Wurman, K. Kosiba, and P. Robinson, 2016: An investigation of the Goshen County,

Wyoming, tornadic supercell of 5 June 2009 using EnKF assimilation of mobile mesonet and radar observations collected during VORTEX2. Part II: Mesocyclone-scale processes affecting tornado formation, maintenance, and decay. *Mon. Wea. Rev.*, **144**, 3441–3463, https://doi.org/10.1175/MWR-D-15-0411.1.

Marshall, T. P., W. Davis, and S. Runnels, 2012: Damage survey of the Joplin tornado. *26th Conf. on Severe Local Storms*, Nashville, TN, Amer. Meteor. Soc., 6.1, https://ams.confex.com/ams/26SLS/webprogram/Paper211662.html.

Mitchell, E. D., S. V. Vasiloff, G. J. Stumpf, A. Witt, M. D. Eilts, J. T. Johnson, and K. W. Thomas, 1998: The National Severe Storms Laboratory tornado detection algorithm. *Wea. Forecasting*, **13**, 352–366, https://doi.org/10.1175/1520-0434(1998)013<0352:TNSSLT>2.0.CO;2.

Parker, M. D., 2014: Composite VORTEX2 supercell environments from near-storm soundings. *Mon. Wea. Rev.*, **142**, 508–529, https://doi.org/10.1175/MWR-D-13-00167.1.

Piltz, S. F., and D. W. Burgess, 2009: The impacts of thunderstorm geometry and WSR-88D beam characteristics on diagnosing supercell tornadoes. *34th Conf. on Radar Meteorology*, Williamsburg, VA, Amer. Meteor. Soc., P6.18, https://ams.confex.com/ams/34Radar/techprogram/paper_155944.htm.

Potvin, C. K., K. L. Elmore, and S. J. Weiss, 2010: Assessing the impacts of proximity sounding criteria on the climatology of significant tornado environments. *Wea. Forecasting*, **25**, 921–930, https://doi.org/10.1175/2010WAF2222368.1.

Rasmussen, E. N., and D. O. Blanchard, 1998: A baseline climatology of sounding-derived supercell and tornado forecast parameters. *Wea. Forecasting*, **13**, 1148–1164, https://doi.org/10.1175/1520-0434(1998)013<1148:ABCOSD>2.0.CO;2.

Ryzhkov, A., T. J. Schuur, D. W. Burgess, and D. S. Zrnić, 2005: Polarimetric tornado detection. *J. Appl. Meteor.*, **44**, 557–570, https://doi.org/10.1175/JAM2235.1.

Schaefer, J. T., and R. Edwards, 1999: The SPC tornado/severe thunderstorm database. Preprints, *11th Conf. on Applied Climatology*, Dallas, TX, Amer. Meteor. Soc., 603–606.

Schultz, C. J., and Coauthors, 2012a: Dual-polarization tornadic debris signatures Part I: Examples and utility in an operational setting. *Electron. J. Oper. Meteor.*, **13**, 120–137.

——, and Coauthors, 2012b: Dual-polarization tornadic debris signatures Part II: Comparisons and caveats. *Electron. J. Oper. Meteor.*, **13**, 138–150.

Smith, B. T., R. L. Thompson, J. S. Grams, C. Broyles, and H. E. Brooks, 2012: Convective modes for significant severe thunderstorms in the contiguous United States. Part I: Storm classification and climatology. *Wea. Forecasting*, **27**, 1114–1135, https://doi.org/10.1175/WAF-D-11-00115.1.

——, ——, A. R. Dean, and P. T. Marsh, 2015: Diagnosing the conditional probability of tornado damage rating using environmental and radar attributes. *Wea. Forecasting*, **30**, 914–932, https://doi.org/10.1175/WAF-D-14-00122.1.

Snyder, J. C., and H. B. Bluestein, 2014: Some considerations for the use of high-resolution mobile radar data in tornado intensity determination. *Wea. Forecasting*, **29**, 799–827, https://doi.org/10.1175/WAF-D-14-00026.1.

——, and A. V. Ryzhkov, 2015: Automated detection of polarimetric tornadic debris signatures using a hydrometeor classification algorithm. *J. Appl. Meteor. Climatol.*, **54**, 1861–1870, https://doi.org/10.1175/JAMC-D-15-0138.1.

Thompson, R. L., R. Edwards, J. A. Hart, K. L. Elmore, and P. Markowski, 2003: Close proximity soundings within supercell environments obtained from the Rapid Update Cycle. *Wea. Forecasting*, **18**, 1243–1261, https://doi.org/10.1175/1520-0434(2003)018<1243:CPSWSE>2.0.CO;2.

——, B. T. Smith, J. S. Grams, A. R. Dean, and C. Broyles, 2012: Convective modes for significant severe thunderstorms in the contiguous United States. Part II: Supercell and QLCS tornado environments. *Wea. Forecasting*, **27**, 1136–1154, https://doi.org/10.1175/WAF-D-11-00116.1.

——, and Coauthors, 2017: Tornado damage rating probabilities derived from WSR-88D data. *Wea. Forecasting*, **32**, 1509–1528, https://doi.org/10.1175/WAF-D-17-0004.1.

Torres, S., and C. Curtis, 2007: Initial implementation of super-resolution data on the NEXRAD network. *23rd Int. Conf. on Interactive Information and Processing Systems for Meteorology, Oceanography, and Hydrology*, San Antonio, TX, Amer. Meteor. Soc., 5B.10, https://ams.confex.com/ams/87ANNUAL/techprogram/paper_116240.htm.

Toth, M., R. J. Trapp, J. Wurman, and K. A. Kosiba, 2013: Comparison of mobile-radar measurements of tornado intensity with corresponding WSR-88D measurements. *Wea. Forecasting*, **28**, 418–426, https://doi.org/10.1175/WAF-D-12-00019.1.

Trapp, R. J., E. D. Mitchell, G. A. Tipton, D. W. Effertz, A. I. Watson, D. L. Andra Jr., and M. A. Magsig, 1999: Descending and nondescending tornadic vortex signatures detected by WSR-88Ds. *Wea. Forecasting*, **14**, 625–639, https://doi.org/10.1175/1520-0434(1999)014<0625:DANTVS>2.0.CO;2.

Van Den Broeke, M. S., and S. T. Jauernic, 2014: Spatial and temporal characteristics of polarimetric tornadic debris signatures. *J. Appl. Meteor. Climatol.*, **53**, 2217–2231, https://doi.org/10.1175/JAMC-D-14-0094.1.

Wakimoto, R. M., and Coauthors, 2016: Aerial damage survey of the 2013 El Reno tornado combined with mobile radar data. *Mon. Wea. Rev.*, **144**, 1749–1776, https://doi.org/10.1175/MWR-D-15-0367.1.

Wood, V. T., and R. A. Brown, 1997: Effects of radar sampling on single-Doppler velocity signatures of mesocyclones and tornadoes. *Wea. Forecasting*, **12**, 928–938, https://doi.org/10.1175/1520-0434(1997)012<0928:EORSOS>2.0.CO;2.

WSEC, 2006: A recommendation for an enhanced Fujita scale (EF-scale). Wind Science and Engineering Center, Texas Tech University, Lubbock, TX, 95 pp., http://www.depts.ttu.edu/weweb/EFScale.pdf.

Wurman, J., and K. Kosiba, 2013: Finescale radar observations of tornado and mesocyclone structures. *Wea. Forecasting*, **28**, 1157–1174, https://doi.org/10.1175/WAF-D-12-00127.1.

——, ——, and P. Robinson, 2013: In situ, Doppler radar, and video observations of the interior structure of a tornado and the wind-damage relationship. *Bull. Amer. Meteor. Soc.*, **94**, 835–846, https://doi.org/10.1175/BAMS-D-12-00114.1.

——, ——, ——, and T. Marshall, 2014: The role of multiple-vortex tornado structure in causing storm researcher fatalities. *Bull. Amer. Meteor. Soc.*, **95**, 31–45, https://doi.org/10.1175/BAMS-D-13-00221.1.

Zrnić, D. S., and R. J. Doviak, 1975: Velocity spectra of vortices scanned with a pulse-Doppler radar. *J. Appl. Meteor.*, **14**, 1531–1539, https://doi.org/10.1175/1520-0450(1975)014<1531:VSOVSW>2.0.CO;2.